

# Mechanisms for the ultralow room-temperature resistivity of SrMoO<sub>3</sub>

Jennifer Coulter,<sup>1</sup> Fabian B. Kugler,<sup>1,2</sup> Harrison LaBollita,<sup>1</sup> Antoine Georges,<sup>1,3,4,5</sup> and Cyrus E. Dreyer<sup>6,1</sup>

<sup>1</sup>*Center for Computational Quantum Physics, Flatiron Institute,  
162 5th Avenue, New York, New York 10010, USA.*

<sup>2</sup>*Institute for Theoretical Physics, University of Cologne, 50937 Cologne, Germany*

<sup>3</sup>*Collège de France, 11 place Marcelin Berthelot, 75005 Paris, France*

<sup>4</sup>*CPHT, CNRS, École Polytechnique, IP Paris, F-91128 Palaiseau, France*

<sup>5</sup>*DQMP, Université de Genève, 24 quai Ernest Ansermet, CH-1211 Genève, Suisse*

<sup>6</sup>*Department of Physics and Astronomy, Stony Brook University, Stony Brook, New York, 11794-3800, USA*

(Dated: June 13, 2025)

SrMoO<sub>3</sub> has one of the lowest experimentally-reported room-temperature resistivities, yet the origin of this property has remained a mystery. Using the Boltzmann transport equation we determine that electron-phonon scattering limits transport at room temperature and is responsible for the approximate  $T^2$  behavior of the resistivity at intermediate temperatures, often attributed to electron-electron Fermi-liquid scattering. We show that the weak electron-phonon coupling, which is similar to, e.g., copper, combined with high electron group velocities for states near the Fermi level, explains the low resistivity of SrMoO<sub>3</sub>. Additionally, the strength of the electron-phonon coupling is found to be sensitive to structural distortions, which may explain disagreements in the literature between single crystal and thin film measurements. The electron-phonon scattering in SrMoO<sub>3</sub> is insensitive to static Coulomb interactions in the partially-filled transition-metal  $d$  orbitals, in contrast to similar oxides such as SrVO<sub>3</sub>. These findings have significant implications for theoretical interpretation of direct-current resistivity in transition-metal oxides and beyond.

The temperature-dependent direct-current (DC) resistivity is one of the most fundamental probes of the electronic properties of materials and is critical to the technological utility of metals. For example, materials with high electrical conductivity at room temperature (RT) and above are important in all electronic devices as contacts and interconnects that allow current to flow with minimal resistance, reducing power consumption and improving heat management [1–3].

Transition-metal oxides, which can feature strong correlations and collective phenomena, also exhibit some of the highest conductivities of any known metals. In particular, the perovskite SrMoO<sub>3</sub> has the eighth lowest reported RT resistivity [4, 5], lower than transition metals like platinum and palladium, and alkali metals like lithium and potassium. However, the origin of the ultralow resistivity of SrMoO<sub>3</sub> has not been established. The DC resistivity,  $\rho$ , exhibits a  $T^2$  temperature dependence in the range of  $\sim 50 - 150$  K, a scaling behavior usually associated with Fermi-liquid (FL) electron-electron (el-el) scattering. However, el-el scattering is highly unlikely to determine transport in a moderately correlated metal at such high  $T$  [6]. Instead, in this regime, electron-phonon (el-ph) scattering is expected to dominate, though the canonical  $T^5$  or  $T$ -linear scaling [7] associated with el-ph scattering is not observed. To complicate matters further, there is only a single report [4] of such superlative conductivity, which also happens to be the only single crystal measurement; thin film results [8–11] show significantly higher RT resistivities.

In this work, we use *ab-initio* el-ph coupling calculations based on density functional theory (DFT) in combination with the Boltzmann transport equation (BTE) to determine the DC transport properties of SrMoO<sub>3</sub>. By

combining our results with DFT plus dynamical mean-field theory (DFT+DMFT) calculations of el-el scattering rates from Ref. 6, we show that el-el scattering is the dominant process only below  $\sim 10$  K. This demonstrates that el-ph scattering determines the resistivity at RT and is responsible for the observed  $\sim T^2$  dependence in the temperature regime up to  $\sim 150$  K. The unexpected temperature scaling can be attributed to the cylindrical shape of the Fermi surface.

We find that the cubic  $Pm\bar{3}m$  structure of SrMoO<sub>3</sub>, expected at RT [12], indeed produces low  $\rho$  on the order of the superlative result of Ref. 4. The low- $T$  orthorhombic  $Imma$  structure, which may be stabilized at RT by epitaxial constraints in thin films [10, 11], results in a somewhat higher value. This suggests that the structure plays a role in the discrepancy between single-crystal and thin-film results. We identify the mechanism of low  $\rho$  through comparison to SrVO<sub>3</sub> (which has a similar electronic structure, but significantly higher RT resistivity) as well as the simple transition metal copper. Such comparisons demonstrate that the ultralow resistivity in SrMoO<sub>3</sub> is a result of low el-ph coupling strength associated with the phonon modes relevant for transport, and that the el-ph coupling for these modes is relatively insensitive to electron correlations.

Transport calculations were performed using the linearized Boltzmann transport equation as implemented in the Phoebe code [13] by iterative solution [14]. To approximate the effects of Coulomb interactions within the transition-metal  $d$  states at the Fermi level, we applied the simplified rotationally-invariant DFT+ $U$  scheme of Dudarev [15] in which an effective  $U_{\text{eff}} = U - J$  is used; following prior work, we choose  $U_{\text{eff}} = 2.76$  eV and 3.85 eV for SrMoO<sub>3</sub> and SrVO<sub>3</sub>, respectively [11, 16–18]. Ad-

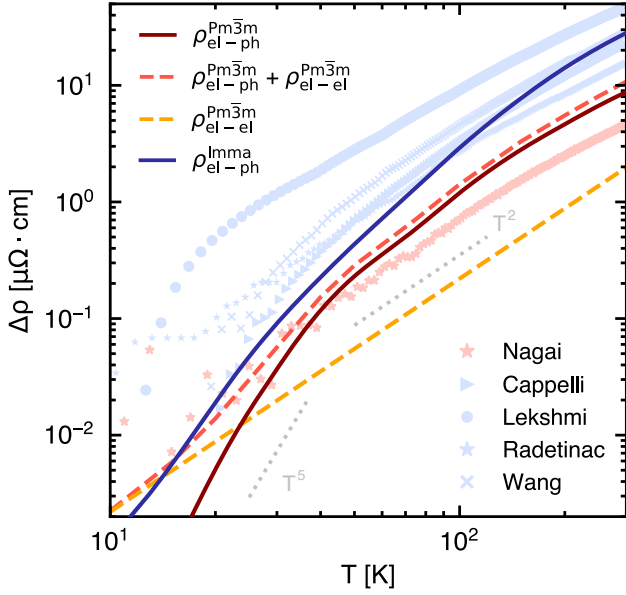


FIG. 1. Direct-current resistivity versus temperature for  $\text{SrMoO}_3$ . The yellow dashed, dark red solid, and light red dashed curves are calculated (DFT+ $U$ +BTE) resistivities from electron-electron (Ref. 6), electron-phonon, and electron-phonon+electron-electron contributions, respectively, for the  $Pm\bar{3}m$  structure. The blue solid curve is the electron-phonon resistivity for the  $Imma$  structure. Light blue points are experimental resistivities for thin films [8–11], and light red for the single crystal [4]. All experimental points have residual resistivities as reported in Ref. 6 subtracted off for comparison to theory. Grey dotted curves are a guide to the eye indicating  $T^5$  and  $T^2$  dependencies.

ditional computational details are found in the End Matter Sec. I. El-el scattering rates were calculated by a subset of the authors in Ref. 6 using DFT+DMFT.

In Fig. 1, we plot  $\rho(T)$  calculated from el-ph scattering for the cubic ( $Pm\bar{3}m$ ) and orthorhombic ( $Imma$ ) crystal structures of  $\text{SrMoO}_3$ . For the cubic case, we also include the contribution from el-el scattering determined from DFT+DMFT [6], and the total, for which we find Matthiessen’s rule to be a good approximation [19] and treat  $\rho_{\text{el-el}}$  and  $\rho_{\text{el-ph}}$  as additive. We compare to experimental data reproduced from the single-crystal measurements of Ref. 4 and the thin-film measurements of Refs. 8–11. In all cases, we removed the residual resistivity contributions according to those determined in Ref. 6 to obtain  $\Delta\rho(T)$ .

We first analyze the RT resistivity values compared with experiment. The resistivity of the cubic structure is lower by a factor of  $\sim 3$  compared to the orthorhombic structure. Interestingly, this is roughly the difference in  $\Delta\rho(300\text{K})$  between the thin-film and the single-crystal experimental results (though there is considerable spread of the data in the former). Based on neutron diffraction of powders, the cubic structure is expected to be the ground state at RT [12]; however, some of the thin films [10, 11] were grown on orthorhombic substrates

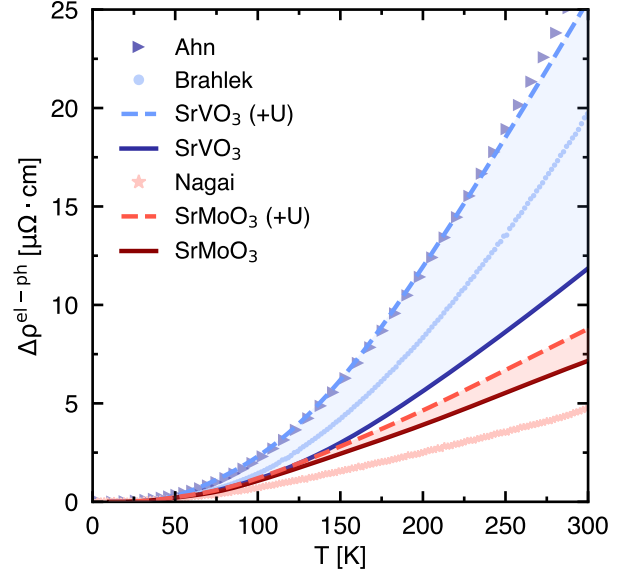


FIG. 2. Comparison of the direct-current resistivity versus temperature of  $\text{SrMoO}_3$  (red) and  $\text{SrVO}_3$  (blue). Solid curves are without a Hubbard  $U$  applied during the calculation, dashed curves have  $U_{\text{eff}} = 2.76$  eV (3.85 eV) for  $\text{SrMoO}_3$  ( $\text{SrVO}_3$ ). Shaded region between solid and dashed curves indicates a rough error range based on the uncertainty in the choice of  $U$ . Light red and blue points are experimental measurements from Refs. 4, 20, 21, plotted with residual resistivities as reported in Ref. 6 subtracted off.

which could stabilize  $Imma$  at RT (Ref. 11 explicitly reported the  $Imma$  structure). Even on cubic substrates, unrelaxed lattice mismatch will cause distortions away from cubic. In principle, the single crystal [4] has no such constraints and is expected to be cubic. We note that our calculation for cubic  $\text{SrMoO}_3$  slightly *overshoots* the experimental results of Ref. 4 (though only by  $\sim 4$   $\mu\Omega\cdot\text{cm}$ ), which could arise from theoretical uncertainties or challenges of obtaining accurate aspect ratios to define  $\rho$  in the single crystal and/or thin films.

We now turn to the temperature dependence of  $\Delta\rho$ , focusing on the cubic case. The most striking feature of the resistivity (both theoretical and experimental) is an approximate  $T^2$  dependence between  $\sim 40 - 150$  K, which has been previously interpreted as the signature of FL el-el scattering. Comparing the  $\rho_{\text{el-ph}}^{Pm\bar{3}m}$  and  $\rho_{\text{el-el}}^{Pm\bar{3}m}$  curves in Fig. 1, we find that the el-ph contribution to  $\Delta\rho(300\text{K})$  is a factor of 4.3 larger than the el-el contribution, and dominates the  $T$  dependence down to  $\sim 40$  K. Then, el-el scattering become relevant to the temperature dependence as the resistivity from el-ph scattering transitions from  $T^2$  to  $T^5$ , with clean FL el-el  $T^2$  behavior appearing around  $\sim 10$  K.

The origin of the unexpected  $\sim T^2$  behavior from el-ph scattering can be explained by the shape of the Fermi surface of  $\text{SrMoO}_3$ , which is characterized by cylinders in each Cartesian direction in reciprocal space [11, 22].

As discussed by Kukkonen [23] and in the End Matter Sec. II, a cylindrical Fermi surface results in three distinct temperature regimes, determined by the dimensions of the cylinder, i.e., its diameter  $2k_r$  and length  $2k_l$ . These define temperature scales  $T_d = \hbar s 2k_r / k_B$  and  $T_l = \hbar s 2k_l / k_B$ , respectively ( $s$  is an isotropic speed of sound in the material). For very low  $T$  ( $T \ll T_d$ ),  $\rho$  is expected to follow a  $T^5$  dependence based on the normal Bloch–Grüneisen (BG) arguments [7, 23] (see End Matter Sec. II). Similarly, for very high  $T$  ( $T \gg T_l, \Theta_D$ , where  $\Theta_D$  is the Debye temperature),  $\rho$  will be proportional to  $T$  since, from BG, the only  $T$  dependence comes from the phonon distribution function, which is linear in  $T$ .

The interesting regime is  $T_d \lesssim T \lesssim T_l$ . Here, large-angle scattering dominates in the radial direction of the cylinder. Assuming deformation-potential-like scattering matrix elements ( $\propto q$ ), the phase space for scattering along the length of the cylinder increases with  $T$ . Finally, the phonon distribution function is also linear in  $T$ , as it depends on the intersection between the phonon sphere (assuming a Debye phonon) of radius  $q_T = k_B / \hbar s$  and the cylindrical Fermi surface, and thus is approximately  $\pi k_r^2 2q_T \propto T$ . Therefore, in total, we have  $\rho(T) \propto T^2$ .

To demonstrate the correspondence of this model and our calculation, we fit our DFT+BTE el-ph resistivity for the  $Pm\bar{3}m$  structure to the model of Ref. 23 in Fig. 4 of the End Matter. We take  $2k_r = 0.6\pi/a$  for the diameter of the cylinder and use the phonon energies/dispersions and deformation potentials as fitting parameters. We obtain an excellent fit, which, unlike the conventional BG expression, can capture the intermediate  $T^2$  regime between  $T^5$  and  $T$ -linear.

Having understood the temperature dependence of  $\rho$ , we turn to the question of greatest interest: why is the RT resistivity so low in SrMoO<sub>3</sub>? We can understand this by considering a simplified isotropic version of the BG equation (applicable at high  $T$ ) [24],  $\rho_{BG}(T) \approx 6\pi V k_B T \lambda_{tr} / e^2 \hbar N_F \langle v^2 \rangle_{FS}$ , where  $V$  is the unit-cell volume,  $\langle v^2 \rangle_{FS}$  is the square of the band velocity averaged over the Fermi surface,  $N_F$  is the electronic density of states (DOS) at the Fermi level, and  $\lambda_{tr}$  is the cumulative isotropic transport el-ph coupling strength [25, 26]. The latter is given by

$$\lambda_{tr} = \frac{1}{N_F} \sum_{mn,\nu} \int_{BZ} \frac{d\mathbf{q}}{V_{BZ}} \int_{BZ} \frac{d\mathbf{k}}{V_{BZ}} \times \frac{1}{\omega_{\mathbf{q}\nu}} |g_{mn,\nu}(\mathbf{k}, \mathbf{q})|^2 \left( 1 - \frac{\mathbf{v}_{\mathbf{k}m} \cdot \mathbf{v}_{\mathbf{k}+\mathbf{q}n}}{|\mathbf{v}_{\mathbf{k}m}| |\mathbf{v}_{\mathbf{k}+\mathbf{q}n}|} \right) \times \delta(\epsilon_{\mathbf{k}m} - \epsilon_F) \delta(\epsilon_{\mathbf{k}+\mathbf{q}n} - \epsilon_F), \quad (1)$$

where  $\mathbf{v}_{\mathbf{k}m}$  is the velocity of band  $m$  and  $k$ -point  $\mathbf{k}$ ,  $\omega_{\mathbf{q}\nu}$  is the frequency of the phonon branch  $\nu$  and wavevector  $\mathbf{q}$ ,  $V_{BZ}$  is the volume of the Brillouin Zone (BZ), and  $\epsilon_F$  the Fermi energy.  $g_{mn,\nu}(\mathbf{k}, \mathbf{q})$  are the electron-phonon

matrix elements,

$$g_{mn,\nu}(\mathbf{k}, \mathbf{q}) = \left( \frac{\hbar}{2m_0 \omega_{\mathbf{q}\nu}} \right)^{1/2} \langle \psi_{\mathbf{k}+\mathbf{q},m} | \partial_{\mathbf{q}\nu} V | \psi_{\mathbf{k}n} \rangle, \quad (2)$$

where  $\psi_{\mathbf{k}n}$ ,  $\psi_{\mathbf{k}+\mathbf{q},m}$  are the Kohn–Sham (KS) wavefunctions at bands  $n, m$  and wavevectors  $\mathbf{k}$ ,  $\mathbf{k} + \mathbf{q}$ ,  $m_0$  a reference mass [27], and  $\partial_{\mathbf{q}\nu} V$  the change in KS potential with the phonon displacement.

	$\frac{N_F}{V} [\text{\AA}^3 \text{eV}]^{-1}$	$\langle v^2 \rangle_{FS} [\frac{m^2}{s^2} 10^{12}]$	$\lambda_{tr}$
Cu	0.024	1.47	0.12
$Pm\bar{3}m$ SrMoO <sub>3</sub>	0.022 (0.021)	0.431 (0.402)	0.13 (0.11)
$Imma$ SrMoO <sub>3</sub>	0.028 (0.028)	0.263 (0.258)	0.17 (0.16)
$Pm\bar{3}m$ SrVO <sub>3</sub>	0.027 (0.027)	0.206 (0.220)	0.19 (0.10)

TABLE I. Density of states at the Fermi level, squared Fermi velocity averaged over the Fermi surface, and isotropic transport el-ph coupling strength for Cu, SrMoO<sub>3</sub> (cubic and orthorhombic), and SrVO<sub>3</sub>, calculated with DFT+ $U$ . Numbers in parentheses are calculated without a Hubbard  $U$ .

In Table I, we provide calculated values for the DOS, band velocities, and  $\lambda_{tr}$  for  $Pm\bar{3}m$  and  $Imma$  SrMoO<sub>3</sub>. We also perform calculations for copper, which has a RT resistivity about a factor of five smaller than what we calculate for cubic SrMoO<sub>3</sub>. Values in parentheses for SrMoO<sub>3</sub> (and SrVO<sub>3</sub>, discussed below) are those calculated without a Hubbard  $U$ , which clearly has a small effect on the results for SrMoO<sub>3</sub>. We see that  $\lambda_{tr}$  for cubic SrMoO<sub>3</sub> is very similar to that of copper, indicating that the mechanism for the superlative RT conductivity on SrMoO<sub>3</sub> is indeed the relatively weak el-ph scattering. We note that  $\lambda_{tr}$  only fully reflects the el-ph scattering in the  $T$ -linear regime above the Debye temperature of the material. For Cu, this is the case at RT [28], while for SrMoO<sub>3</sub> it occurs at somewhat higher  $T$  (see End Matter Fig. 4); therefore, the el-ph scattering relevant for RT resistivity in SrMoO<sub>3</sub> is even slightly smaller than indicated by  $\lambda_{tr}$ . From Table I, the reason Cu is more conductive at RT is due to its much larger band velocity; the DOS at the Fermi level is similar between Cu and SrMoO<sub>3</sub>. Also,  $Imma$  SrMoO<sub>3</sub> has significantly higher RT resistivity than  $Pm\bar{3}m$  due to a somewhat larger  $\lambda_{tr}$  and a reduced band velocity caused by the symmetry-lowering octahedral distortions (see End Matter Secs. III and IV).

To gain insight into the weak el-ph scattering in SrMoO<sub>3</sub>, we compare to SrVO<sub>3</sub>, which has a similar electronic structure (see End Matter Fig. 5), but a somewhat higher measured resistivity [20–22, 29–39]. (There are still significant open questions about the experimental RT resistivity of SrVO<sub>3</sub> [6], but the lowest reported value is  $20 \mu\Omega \cdot \text{cm}$  [35].) It was also found that the el-el scattering rate in these two materials calculated from DFT+DMFT is almost identical [6], and therefore we expect similar strength of the electron correlations. In

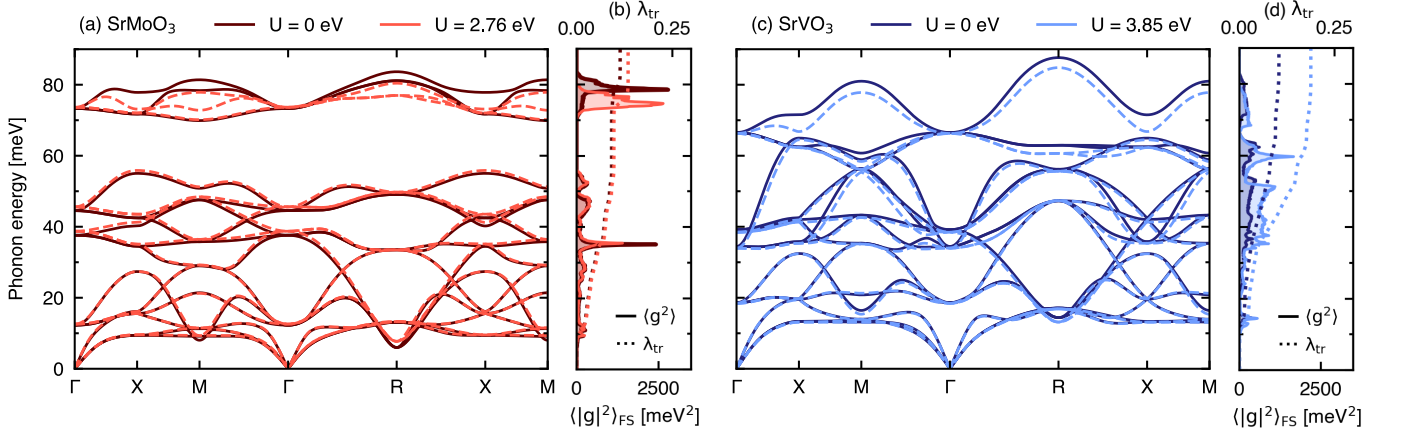


FIG. 3. Phonon dispersion for (a) SrMoO<sub>3</sub> and (c) SrVO<sub>3</sub> with and without Hubbard  $U$ . Panels (b) and (d) show the el-ph matrix elements averaged over the Fermi surface given by Eq. (3) (solid curves) and isotropic transport el-ph coupling strength  $\lambda_{tr}$  given by Eq. (1) resolved over phonon frequencies (dashed curves) versus phonon energy for SrMoO<sub>3</sub> and SrVO<sub>3</sub>, respectively.

Fig. 2, we compare the el-ph resistivities for SrMoO<sub>3</sub> and SrVO<sub>3</sub>. Interestingly, if no Hubbard  $U$  is applied, the two materials both show somewhat similar  $\rho(T)$  values, with SrMoO<sub>3</sub> around  $\sim 7 \mu\Omega \cdot \text{cm}$  and SrVO<sub>3</sub>  $\sim 12 \mu\Omega \cdot \text{cm}$  at RT, where the modest difference between these values is the result of the larger band velocity and smaller  $\lambda_{tr}$  of SrMoO<sub>3</sub>. Adding an effective Hubbard  $U$  has a small effect on SrMoO<sub>3</sub> ( $\sim 10\%$  increase) but causes a large increase for SrVO<sub>3</sub>; the latter's RT resistivity more than doubles, to a value much closer to the experimental one (a similar conclusion was reached in Ref. 40). Therefore, it is clear that the weak dependence of resistivity on electron correlations plays a key role in the lower RT  $\rho$  of SrMoO<sub>3</sub>.

Generally, the fact that adding a Hubbard  $U$  causes substantial changes is somewhat surprising. Our calculations are spinless (reflecting the lack of magnetic order in these materials), and the cubic symmetry implies that the  $t_{2g}$  orbitals are degenerate. Therefore, the addition of  $U$  should have little effect on the electronic structure. Indeed, as we show in the End Matter, Sec. III, there is no substantive change in the electronic band structure of either SrMoO<sub>3</sub> or SrVO<sub>3</sub> upon adding  $U$ . Similarly, the phonon band structures also do not change substantially [Fig. 3(a) and (c)]. This makes it unlikely that scattering phase space changes are responsible for the change in  $\rho$  for either material.

Instead, what we find changes significantly with  $U$  are the el-ph matrix elements  $g_{mn,\nu}(\mathbf{k}, \mathbf{q})$  [Eq. (2)]. This can be seen in Fig. 3(b) and (d), where we plot the matrix elements averaged over the Fermi surface,

$$\langle |g|^2 \rangle_{FS}(\omega) = \sum_{mn,\nu} \int_{BZ} \frac{d\mathbf{q}}{V_{BZ}} \int_{BZ} \frac{d\mathbf{k}}{V_{BZ}} |g_{mn,\nu}(\mathbf{k}, \mathbf{q})|^2 \times \delta(\epsilon_{n\mathbf{k}} - \epsilon_F) \delta(\epsilon_{m\mathbf{k}+\mathbf{q}} - \epsilon_F) \delta(\omega - \omega_{\mathbf{q}\nu}), \quad (3)$$

as well as the isotropic  $\lambda_{tr}$  resolved with respect to the

phonon frequency. Comparing the curves with and without  $U$  shows that, for SrMoO<sub>3</sub>, the changes to the el-ph matrix elements are modest and mostly occur in the highest-energy optical branches ( $\omega > 70$  meV), which are less relevant for  $T \leq 300$  K transport. However, for SrVO<sub>3</sub>, there is a significant enhancement of the matrix elements between 30 – 70 meV, as well as a slight enhancement of those in the 10 – 30 meV range, upon the addition of  $U$  (this was also reported in Ref. 40, 41), which causes the large change in  $\rho$  of SrVO<sub>3</sub> in Fig. 2. This change is quantified in Table I, where we see a factor of  $\sim 2$  increase in  $\lambda_{tr}$  for SrVO<sub>3</sub> with the addition of  $U$  to a value  $\sim 1.5$  times that of cubic SrMoO<sub>3</sub>. This, in addition to the twice smaller band velocity term for SrVO<sub>3</sub> (from the narrower band width, see End Matter Fig. 5) accounts for the factor of  $\sim 3$  difference between RT resistivities of the two materials.

The phonon modes most affected by  $U$  are, for both materials, the optical modes that couple most strongly to the breaking of the  $t_{2g}$  orbital degeneracy of the cubic structure. For example, Fig. 7 in the End Matter Sec. V plots the electronic band structure of SrMoO<sub>3</sub> with the eigen-displacements of the three highest frequency M-point modes (labeled as  $\nu = 13, 14, 15$ ) frozen into the structure. We can clearly see that the  $\nu = 14$  mode, whose el-ph coupling is most affected by the inclusion of  $U$ , causes significant splitting of electronic degeneracies at the Fermi level. In contrast,  $\nu = 13$  does not cause such splittings, and is therefore much less affected by  $U$ .

In conclusion, we demonstrate that the superlative conductivity of cubic SrMoO<sub>3</sub> arises from weak el-ph scattering, which dominates its resistivity at RT, and produces an unexpected  $T^2$  dependence at intermediate  $T$  due to the cylindrical shape of the Fermi surface. The el-ph scattering is relatively insensitive to correlation effects at the level of DFT+ $U$ , contrary to the case of the related material SrVO<sub>3</sub>. The orthorhombic phase



of SrMoO<sub>3</sub> shows higher  $\rho$  due to a slightly larger overall el-ph coupling and lower bandwidth, which we identify as a possible reason for the difference in resistivity measured in thin films versus single crystals.

These results suggest design principles for finding other high-conductivity oxides, indicating high symmetry structures and stiff metal-oxygen bonds may reduce the effects of the band-splitting modes on transport. In addition, the unexpected temperature scaling of the resistivity serves as a word of caution when interpreting high-temperature  $T^2$  as arising from Fermi-liquid electron-electron scattering. Finally, this case study of resistivity in SrMoO<sub>3</sub> versus SrVO<sub>3</sub> indicates the importance of including correlation effects beyond DFT in *ab-initio* el-ph coupling calculations.

## ACKNOWLEDGMENTS

We are grateful to Andy Millis, Jernej Mravlje, Sophie Beck, David Abramovitch and Philip Allen for useful discussions. We thank Naoki Shirakawa for sending us the data of Ref. 4. C.E.D. acknowledges support from the National Science Foundation under Grant No. DMR-2237674. F.B.K. acknowledges funding from the Ministry of Culture and Science of the German State of North Rhine-Westphalia (NRW Rückkehrprogramm). The Flatiron Institute is a division of the Simons Foundation.

- 
- [1] D. Gall, The search for the most conductive metal for narrow interconnect lines, *J. Appl. Phys.* **127**, 050901 (2020).
  - [2] D. Gall, J. J. Cha, Z. Chen, H.-J. Han, C. Hinkle, J. A. Robinson, R. Sundararaman, and R. Torsi, Materials for interconnects, *MRS Bull.* **46**, 959 (2021).
  - [3] J.-S. Kim, J. Kim, D.-J. Yang, J. Shim, L. Hu, C. Lee, J. Kim, and S. W. Kim, Addressing interconnect challenges for enhanced computing performance, *Science* **386**, eadk6189.
  - [4] I. Nagai, N. Shirakawa, S. I. Ikeda, R. Iwasaki, H. Nishimura, and M. Kosaka, Highest conductivity oxide SrMoO<sub>3</sub> grown by a floating-zone method under ultralow oxygen partial pressure, *App. Phys. Lett.* **87**, 2 (2005).
  - [5] A. P. Mackenzie, The properties of ultrapure delafossite metals, *Rep. Prog. Phys.* **80**, 032501 (2017).
  - [6] F. B. Kugler, J. Lee-Hand, H. LaBollita, L. V. Muñoz, J. Kaye, S. Beck, A. Hampel, A. Georges, and C. E. Dreyer, Fermi-liquid  $T^2$  resistivity: Dynamical mean-field theory meets experiment, [arXiv:2412.16363](https://arxiv.org/abs/2412.16363) (2025).
  - [7] J. Ziman, *Electrons and phonons: the theory of transport phenomena in solids* (Oxford university press, 1960).
  - [8] H. Wang, D. Cui, Y. Zhou, Z. Chen, F. Chen, T. Zhao, H. Lu, G. Yang, M. Xu, Y. Lan, X. Chen, H. Qian, and F. Liu, Growth and characterization of SrMoO<sub>3</sub> thin films, *J. Crys. Growth* **226**, 261 (2001).
  - [9] I. C. Lekshmi, A. Gayen, and M. Hegde, The effect of strain on nonlinear temperature dependence of resistivity in SrMoO<sub>3</sub> and SrMoO<sub>3-x</sub>N<sub>x</sub> films, *MRS Bull.* **40**, 93 (2005).
  - [10] A. Radetinac, J. Zimmermann, K. Hoyer, H. Zhang, P. Komissinskiy, and L. Alff, Optical properties of single crystalline SrMoO<sub>3</sub> thin films, *J. App. Phys.* **119**, 055302 (2016).
  - [11] E. Cappelli, A. Hampel, A. Chikina, E. B. Guedes, G. Gatti, A. Hunter, J. Issing, N. Biskup, M. Varela, C. E. Dreyer, A. Tamai, A. Georges, F. Y. Bruno, M. Radovic, and F. Baumberger, Electronic structure of the highly conductive perovskite oxide SrMoO<sub>3</sub>, *Phys. Rev. Mater.* **6**, 075002 (2022).
  - [12] B. Macquart, B. J. Kennedy, and M. Avdeev, Neutron diffraction study of phase transitions in perovskite-type strontium, *J. of Solid State Chem.* **183**, 249 (2010).
  - [13] A. Cepellotti, J. Coulter, A. Johansson, N. S. Fedorova, and B. Kozinsky, Phoebe: a high-performance framework for solving phonon and electron Boltzmann transport equations, *J. Phys. Mater.* **5**, 035003 (2022).
  - [14] M. Omini and A. Sparavigna, An iterative approach to the phonon boltzmann equation in the theory of thermal conductivity, *Physica B* **212**, 101 (1995).
  - [15] S. L. Dudarev, G. A. Botton, S. Y. Savrasov, C. J. Humphreys, and A. P. Sutton, Electron-energy-loss spectra and the structural stability of nickel oxide: An LSDA+U study, *Phys. Rev. B* **57**, 1505 (1998).
  - [16] J. Lee-Hand, A. Hampel, and C. E. Dreyer, First-principles study of the electronic, magnetic, and crystal structure of perovskite molybdates, *Phys. Rev. Mater.* **5**, 085001 (2021).
  - [17] A. Hampel, S. Beck, and C. Ederer, Effect of charge self-consistency in DFT + DMFT calculations for complex transition metal oxides, *Phys. Rev. Res.* **2**, 033088 (2020).
  - [18] F. Lechermann, A. Georges, A. Poteryaev, S. Biermann, M. Posternak, A. Yamasaki, and O. K. Andersen, Dynamical mean-field theory using Wannier functions: A flexible route to electronic structure calculations of strongly correlated materials, *Phys. Rev. B* **74**, 125120 (2006).
  - [19] In this instance, adding the DMFT Fermi-liquid el-el scattering rate to the el-ph rate within the relaxation-time approximation produces the same result as adding  $\rho_{\text{DMFT}}$  and  $\rho_{\text{el-ph}}$  calculated separately using the RTA level. However, in the main manuscript, we use an iterative solution to the linearized BTE, which takes into account the full electron scattering matrix in the solution of the BTE. Here, our DMFT el-el scattering rate only provides momentum-independent “out” scattering, representing the diagonal contribution to the scattering matrix, rather than a full scattering-matrix contribution. To avoid violating conservation of charge in the full scattering-matrix BTE calculation, we calculate and add these contributions to  $\rho$  separately.
  - [20] G. Ahn, M. Zingl, S. J. Noh, M. Brahelek, J. D. Roth, R. Engel-Herbert, A. J. Millis, and S. J. Moon, Low-energy interband transition in the infrared response of the correlated metal SrVO<sub>3</sub> in the ultraclean limit, *Phys. Rev. B* **106**, 085133 (2022).

- [21] M. Brahlek, L. Zhang, C. Eaton, H.-T. Zhang, and R. Engel-Herbert, Accessing a growth window for SrVO<sub>3</sub> thin films, *App. Phys. Lett.* **107**, 143108 (2015).
- [22] M. Mirjolet, F. Rivadulla, P. Marsik, V. Borisov, R. Valentí, and J. Fontcuberta, Electron-phonon coupling and electron-phonon scattering in SrVO<sub>3</sub>, *Adv. Sci.* **8**, 2004207 (2021).
- [23] C. A. Kukkonen,  $T^2$  electrical resistivity due to electron-phonon scattering on a small cylindrical Fermi surface: Application to bismuth, *Phys. Rev. B* **18**, 1849 (1978).
- [24] P. B. Allen and W. H. Butler, Electrical conduction in metals, *Phys. Today* **31**, 44 (1978).
- [25] G. Grimvall, *Thermophysical properties of materials* (Elsevier, 1999).
- [26] S. Poncé, E. Margine, C. Verdi, and F. Giustino, EPW: Electron-phonon coupling, transport and superconducting properties using maximally localized wannier functions, *Comput. Phys. Commun.* **209**, 116 (2016).
- [27] F. Giustino, M. L. Cohen, and S. G. Louie, Electron-phonon interaction using wannier functions, *Phys. Rev. B* **76**, 165108 (2007).
- [28] R. A. Matula, Electrical resistivity of copper, gold, palladium, and silver, *J. Phys. Chem. Ref. Data* **8**, 1147 (1979).
- [29] D. Reyes Ardila, J. Andreeta, and H. Basso, Preparation, microstructural and electrical characterization of SrVO<sub>3</sub> single crystal fiber, *J. Crys. Growth* **211**, 313 (2000).
- [30] I. H. Inoue, O. Goto, H. Makino, N. E. Hussey, and M. Ishikawa, Bandwidth control in a perovskite-type  $3d^1$ -correlated metal Ca<sub>1-x</sub>Sr<sub>x</sub>VO<sub>3</sub>. I. Evolution of the electronic properties and effective mass, *Phys. Rev. B* **58**, 4372 (1998).
- [31] T. Berry, S. Bernier, G. Auffermann, T. M. McQueen, and W. Adam Phelan, Laser floating zone growth of SrVO<sub>3</sub> single crystals, *J. Crys. Growth* **583**, 126518 (2022).
- [32] R. Xu, Y. Ji, R. Bouchilaoun, F. Qian, M. Li, X. Zhang, R. Tang, R. Zhao, S. Misra, H. Wang, W. Li, C. Kan, D. Shi, J. Fan, and H. Yang, Optical and electrical properties of (111)-oriented epitaxial SrVO<sub>3</sub> thin films, *Ceram. Int.* **45**, 11304 (2019).
- [33] J. Roth, T. Kuznetsova, L. Miao, A. Pogrebnnyakov, N. Alem, and R. Engel-Herbert, Self-regulated growth of [111]-oriented perovskite oxide films using hybrid molecular beam epitaxy, *APL Mater.* **9**, 021114 (2021).
- [34] A. Fouchet, M. Allain, B. Bérini, E. Popova, P.-E. Janolin, N. Guiblin, E. Chikoidze, J. Scola, D. Hrabovsky, Y. Dumont, and N. Keller, Study of the electronic phase transition with low dimensionality in SrVO<sub>3</sub> thin films, *Mater. Sci. Eng. B* **212**, 7 (2016).
- [35] M. Brahlek, J. D. Roth, L. Zhang, M. Briggeman, P. Irvin, J. Lapano, J. Levy, T. Birol, and R. Engel-Herbert, Hidden transport phenomena in an ultraclean correlated metal, *Nat. Commun.* **15**, 5304 (2024).
- [36] L. Shoham, M. Baskin, M.-G. Han, Y. Zhu, and L. Kornblum, Scalable synthesis of the transparent conductive oxide SrVO<sub>3</sub>, *Adv. Electron. Mater.* **6**, 1900584 (2020).
- [37] L. Zhang, Y. Zhou, L. Guo, W. Zhao, A. Barnes, H.-T. Zhang, C. Eaton, Y. Zheng, M. Brahlek, H. F. Haneef, N. J. Podraza, M. H. Chan, V. Gopalan, K. M. Rabe, and R. Engel-Herbert, Correlated metals as transparent conductors, *Nat. Mater.* **15**, 204 (2016).
- [38] M. Mirjolet, F. Sánchez, and J. Fontcuberta, High carrier mobility, electrical conductivity, and optical transmittance in epitaxial SrVO<sub>3</sub> thin films, *Adv. Funct. Mater.* **29**, 1808432 (2019).
- [39] M. Mirjolet, H. B. Vasili, A. Valadkhani, J. Santiso, V. Borisov, P. Gargiani, M. Valvidares, R. Valentí, and J. Fontcuberta, Orbital occupancy and hybridization in strained SrVO<sub>3</sub> epitaxial films, *Phys. Rev. Mater.* **5**, 095002 (2021).
- [40] D. J. Abramovitch, J. Mravlje, J.-J. Zhou, A. Georges, and M. Bernardi, Respective roles of electron-phonon and electron-electron interactions in the transport and quasiparticle properties of SrVO<sub>3</sub>, *Phys. Rev. Lett.* **133**, 186501 (2024).
- [41] D. J. Abramovitch, J. Coulter, S. Beck, and A. Millis, Electron-phonon coupling in correlated metals: A dynamical mean-field theory study, arXiv preprint arXiv:2505.03958 (2025).
- [42] R. Sundararaman, K. Letchworth-Weaver, K. A. Schwarz, D. Gunceler, Y. Ozhables, and T. Arias, JDFTx: Software for joint density-functional theory, *SoftwareX* **6**, 278 (2017).
- [43] D. R. Hamann, Optimized norm-conserving vanderbilt pseudopotentials, *Phys. Rev. B* **88**, 085117 (2013).
- [44] J. P. Perdew, K. Burke, and M. Ernzerhof, Generalized gradient approximation made simple, *Phys. Rev. Lett.* **77**, 3865 (1996).

## END MATTER

### I. COMPUTATIONAL DETAILS

DFT and electron-phonon calculations were performed with the JDFTx open-source plane-wave density functional theory code [42], utilizing the Optimized Norm-Conserving Vanderbilt pseudopotentials [43] parameterized for the Perdew-Burke-Ernzerhof (PBE) [44] exchange-correlation functional for all calculations. For SrMoO<sub>3</sub> and SrVO<sub>3</sub>, we used 35 Hartree plane-wave energy cutoffs, with a  $12 \times 12 \times 12$  k-point mesh and a  $4 \times 4 \times 4$  phonon supercell for cubic structure calculations, and an  $8 \times 8 \times 8$  k-point mesh and  $4 \times 4 \times 4$  phonon supercell for SrMoO<sub>3</sub> in the orthorhombic structure. For copper, we applied an effective  $U = 2$  eV, a 40 Hartree plane-wave coefficient cutoff, and a  $20 \times 20 \times 20$  k-mesh and  $5 \times 5 \times 5$  phonon supercell.

Boltzmann transport calculations were performed using the open-source Phoebe code [13] by solving the BTE using an iterative solution. Adaptive Gaussian smearing was used to broaden the Dirac delta functions appearing in transport calculations. Calculations were converged using fine k-mesh grids from  $75 \times 75 \times 75$  at 300 K and increasing to  $165 \times 165 \times 165$  at 10 K.

### II. $T^2$ RESISTIVITY FROM ELECTRON-PHONON SCATTERING ON A CYLINDRICAL FERMI SURFACE

As discussed in the main text, the most striking feature of the experimental and theoretical resistivity is the approximate  $T^2$  dependence arising from el-ph scattering. To demonstrate how this can be caused by a cylindrical Fermi surface, we compare in this section our full DFT+BTE calculations to the the model of Kukkonen [23], which assumes a cylindrical Fermi surface, as well as to the conventional Bloch-Grüneisen equation [7], which assumes a spherical Fermi surface. The general argument is as follows. We can write the resistivity as

$$\rho = \langle |g(\mathbf{k}, \mathbf{q})|^2 n(\mathbf{q})(1 - \cos \theta) \rangle, \quad (4)$$

where  $g(\mathbf{k}, \mathbf{q})$  is the el-ph matrix element,  $n(\mathbf{q})$  is the phonon distribution function, and the  $1 - \cos \theta$  factor isolates the high-angle scattering that degrades the current. We assume an isotropic Debye model for phonons characterized by a speed of sound  $s$  and Debye temperature  $\Theta_D = \hbar s Q_D / k_B$  ( $Q_D$  is the Debye wavevector). The scattering is taken to be deformation-potential-like,  $|g(\mathbf{k}, \mathbf{q})|^2 \propto q$  [7], and the Fermi surface is a single cylindrical sheet with a diameter in reciprocal space of  $2k_r$  and a length  $2k_l > 2k_r$ . Thus, we can define three

temperature regimes. The first is  $T \ll T_r, \Theta_D$  where  $T_r = \hbar s 2k_r / k_B$ ; in this case, the maximum wavevector of the available phonons scales like  $T$ , so all  $q$  dependence becomes  $T$  dependence. Specifically,  $|g(\mathbf{k}, \mathbf{q})|^2 \propto T$  and  $(1 - \cos \theta) \propto T^2$  [7]. The phonons that are allowed by energy and momentum to scatter lie on the intersection of the Fermi surface and the phonon sphere (the latter with radius  $q_T = k_B / \hbar s$ ). For  $q_T \ll k_r \ll k_l$ , this intersection is a disk of area  $\pi q_T^2$ , and thus  $n(\mathbf{q}) \propto T^2$ . Putting this all together gives the conventional  $T^5$  scaling. At very high temperatures  $T \gg \Theta_D, T_r, T_l$ , the only  $T$  dependence is from the distribution function, which is linear in  $T$ .

The interesting  $T$  regime is  $T_r \lesssim T \lesssim T_l$ . In this case, there are sufficient phonon wavevectors for large-angle scattering across the cylinder, so  $(1 - \cos \theta)$  does not give any  $T$  dependence. However,  $|g(\mathbf{k}, \mathbf{q})|^2$  still contributes a factor of  $T$  since increasing  $q$  allows more scattering along the length of the cylinder. Finally, the intersection with the phonon sphere and the Fermi surface is the cylindrical surface  $\pi k_r^2 2q_T \propto T$  (neglecting the ends of the cylinder). Thus, the total dependence is  $T^2$ .

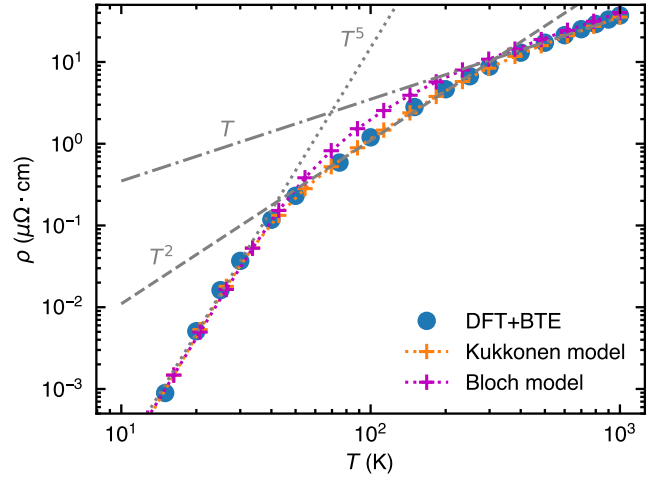


FIG. 4. *Ab-initio* density functional theory plus Boltzmann transport equation (solved via iterative diagonalization) data for the temperature-dependent resistivity of SrMoO<sub>3</sub> (blue circles) fit to the model of Ref. 23 Eq. (5), (magenta +’s) which assumes a cylindrical Fermi surface, and the conventional Bloch-Grüneisen formula Eq. (6) (orange +’s), which assumes a spherical Fermi surface. Gray lines are guides to the eye for different  $T$  scalings.

In Ref. 23, the following expression for the resistivity was derived using the variational method that leads to the conventional Bloch-Grüneisen equation (see below) [7] but assuming a cylindrical Fermi surface (and neglecting Umklapp processes):

$$\rho(T) = \frac{9(m^*)^2 C^2}{64\pi^4 \hbar e^2 M n^2 k_B T} \int_0^{2k_r} \frac{q_\perp^2 dq_\perp}{\sqrt{1 - (q_\perp/2k_r)^2}} \int_{q_\perp}^{q_{\max}} \frac{q^3 dq}{\sqrt{q^2 - q_\perp^2} (1 - e^{-\hbar\omega(q)/k_B T}) (e^{\hbar\omega(q)/k_B T} - 1)}, \quad (5)$$

where  $m^*$  is the effective mass (we estimate  $1.25 m_e$ ),  $C$  is the deformation potential (we take this to be a fitting parameter),  $M = 5.66 \text{ g/cm}^3$  is the mass density,  $n = 2/V$  is the charge density ( $V$  is the cell volume),  $\omega(q)$  is the phonon dispersion, and  $q_{\text{max}}$  is the lesser of  $Q_D$  and  $\sqrt{(2k_l)^2 + q_{\perp}^2}$ ; from the Fermi surface of  $\text{SrMoO}_3$ , we take (roughly)  $2k_r = 0.6\pi/a$  and  $2k_l = 2\pi/a$ . Note the minus sign in the exponent of the first exponential factor, which is missing in Ref. 23 (we attribute this to a typo in that work). To obtain a good fit with the DFT+BTE data, we approximate the full phonon dispersion with one Debye phonon mode characterized by speed of sound  $s = 5101 \text{ m/s}$  (thus  $\Theta_D = 26 \text{ meV}$ ) compared to  $s \simeq 4300 \text{ m/s}$  estimated from DFT, and one Einstein mode with energy of  $60 \text{ meV}$ . For the Debye mode, our fit gives  $C = 40 \text{ eV}$  for the Debye mode and  $C = 150 \text{ eV}$  for the Einstein mode. We note that the somewhat unphysical values of  $C$  are likely related to the inclusion of just two simplified phonon modes as well as the simplified Fermi surface assumed. In any case,  $C$  will not enter into the temperature dependence, which is our focus. In Fig. 4, we compare this model with our data showing that we achieve a quantitative fit.

We can compare this with a fit to the conventional Bloch–Grüneisen formula which assumes a spherical Fermi surface. Then, the resistivity is given by [7]

$$\rho(T) = \frac{(m^*)^2 C^2}{12\pi^3 \hbar e^2 M n^2 k_B T} \times \int_0^{Q_D} \frac{q^5 dq}{(1 - e^{-\hbar\omega(q)/k_B T})(e^{\hbar\omega(q)/k_B T} - 1)}. \quad (6)$$

With similar parameters (the only necessary difference for obtaining a good fit to the data is that  $C$  for the Einstein mode is set to  $40 \text{ eV}$  and the speed of sound is adjusted to  $5780 \text{ m/s}$ ), we can also achieve a satisfactory fit of the DFT data (Fig. 4). However, there is a clear overshooting at intermediate temperatures caused by the direct transition between  $T^5$  and  $T$  scaling, with no intermediate  $T^2$  regime. This analysis demonstrates that the  $T^2$  behavior in the resistivity at intermediate temperatures can be directly attributed to the cylindrical shape of the Fermi surface.

### III. ELECTRONIC STRUCTURE OF $\text{SrMoO}_3$ AND $\text{SrVO}_3$

As discussed in the main text,  $\text{SrMoO}_3$  and  $\text{SrVO}_3$  have similar electronic structures, with  $B$ -site transition metal  $t_{2g}$  states around the Fermi level, see Fig. 5(a) and (b) for the cubic cases.  $\text{SrVO}_3$  is  $d^1$  while  $\text{SrMoO}_3$  is  $d^2$ , and has about twice the bandwidth of  $\text{SrVO}_3$ . This contributes to the enhanced conductivity, see Table I. The orthorhombic  $Imma$  structure of  $\text{SrMoO}_3$ , whose band structure is shown in Fig. 5(c) has a somewhat reduced bandwidth for the  $t_{2g}$  states, which is partially responsible for the higher resistivity.

From Fig. 5, the addition of a Hubbard  $U$  does not cause significant changes in the bandstructures, which is expected for the nonmagnetic case.

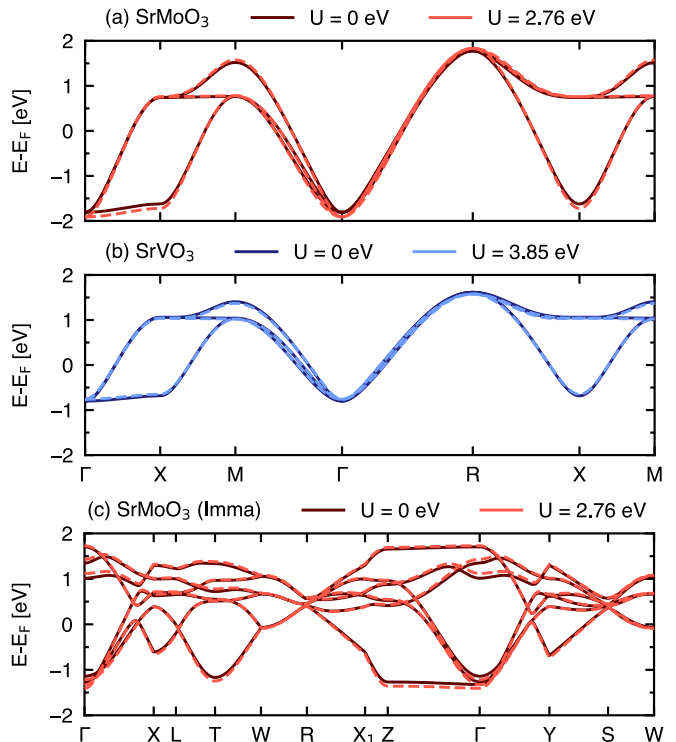


FIG. 5. Band structures for (a)  $Pm\bar{3}m$   $\text{SrMoO}_3$ , (b)  $Pm\bar{3}m$   $\text{SrVO}_3$ , and (c)  $Imma$   $\text{SrMoO}_3$  with and without an effective Hubbard  $U$  applied.

### IV. ELECTRON-PHONON COUPLING IN ORTHORHOMBIC STRUCTURE OF $\text{SrMoO}_3$

In Fig. 6(a) we plot the phonon dispersion for  $Imma$   $\text{SrVO}_3$ . Similarly to the  $Pm\bar{3}m$  case, shown in Fig. 3, the addition of a Hubbard  $U$  does not significantly change the phonon dispersion, though there are some shifts of the high-energy optical modes. The electron-phonon coupling averaged over the Fermi surface [Eq. (3)] and el-ph coupling strength [Eq. (1)] are given in Fig. 6(b) for  $Imma$ ; for comparison, the results for  $Pm\bar{3}m$   $\text{SrMoO}_3$  are reproduced in panel (c) from Fig. 3(b). We see that the overall  $\lambda_{\text{tr}}$  is slightly larger for  $Imma$ , and the optical modes are slightly softened due to the weakening of the Mo-O bonds by the octahedral tilts, making them more relevant to transport at intermediate temperatures. The effect of the Hubbard  $U$  on the el-ph matrix elements is similar between the two structures.



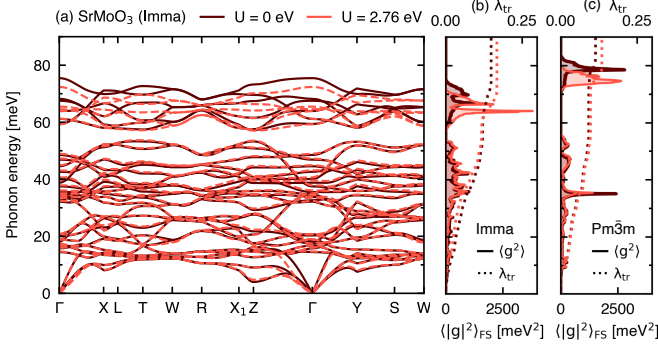


FIG. 6. (a) Phonon dispersion of the orthorhombic  $Imma$  structure of  $SrMoO_3$  with and without an effective Hubbard  $U$ . Electron-phonon matrix elements averaged over the Fermi surface given by Eq. (3) (solid curves) and isotropic transport el-ph coupling strength  $\lambda_{tr}$  given by Eq. (1) resolved over phonon frequencies (dashed curves) versus phonon energy for (b)  $Imma$  and (c)  $Pm\bar{3}m$ .

## V. EFFECT OF HUBBARD $U$ ON PHONON-INDUCED BAND SPLITTING

From Figs. 3 and 6, it is clear that the high-energy optical modes in  $SrMoO_3$  are the ones most affected by the addition of a Hubbard  $U$ , and are responsible for the changes in the el-ph coupling strength. To better understand why this is, we focus on the M-point and compare the three highest frequency modes,  $\nu = 13, 14, 15$ . We choose these modes because we observe that at the M-point, the  $\nu = 14$  mode shows the largest changes in el-ph coupling, while the other two optical modes are only slightly modified. We inspect the change of the electron-phonon matrix elements associated with these phonon modes with the addition of  $U$ , i.e.,  $\sum_{k,mn} [|g_{mn,\nu}^{DFT+U}(\mathbf{k}, \mathbf{q} = M)| - |g_{mn,\nu}^{DFT}(\mathbf{k}, \mathbf{q} = M)|]$ , and find an increase of 1.5, 90.4, and 26.7 meV for  $\nu = 13, 14, 15$ , respectively.

In Fig. 7(a)-(c), we plot the electronic band structure of a  $2 \times 2 \times 2$   $SrMoO_3$  supercell with distortions from the  $\nu = 13, 14, 15$  modes frozen in [see panels (d)-(f) for distortion patterns]. Clearly,  $\nu = 14$  couples most strongly to the splitting of bands around the Fermi level, as it involves distortions of the O octahedra, thus lowering the symmetry of the crystal field felt by the Mo

$d$  orbitals. In terms of the symmetry,  $\nu = 14$  transforms like the  $B_{1g}$  irreducible representation of the  $4/mmm$  little group at the M point (i.e.,  $M_2$ ). This mode will couple to the splitting of degenerate electronic states with  $E_g$  symmetry (or  $T_{2g}$ , but note that apart from the  $\Gamma$  and R points, the highest degeneracy of the electronic states will be two-fold). The magnitude of the splitting is enhanced by the inclusion of  $U$  in the calculation.

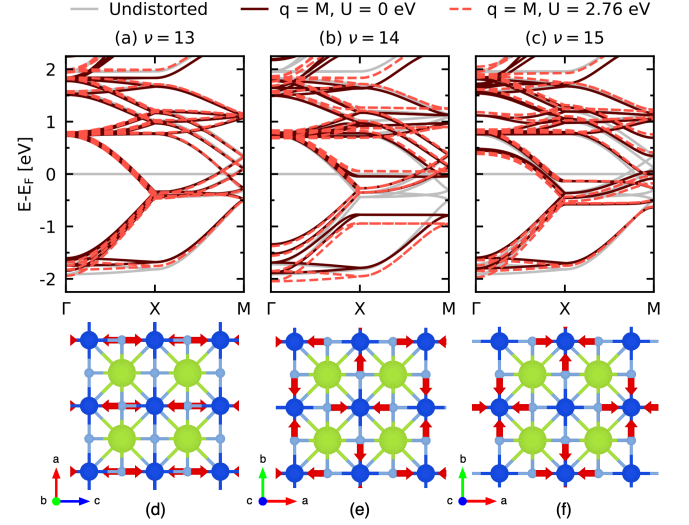


FIG. 7. Electronic band structures of  $SrMoO_3$  with the M-point optical phonon modes frozen into the crystal structure, with and without an effective Hubbard  $U$ . Shown are the (a) third highest, (b) second highest and (c) highest energy phonon modes, along with their respective phonon eigen-displacements shown in (d), (e), (f). Note that here, to accommodate the M-point phonon displacements, the bands are plotted using a  $2 \times 2 \times 2$  supercell with high symmetry labels corresponding to the supercell structure.

Mode  $\nu = 15$ , which has  $A_{1g}$  ( $M_1$ ) symmetry also results in some splittings around the Fermi level, which explains why it also has a nonnegligible change with  $U$ . This mode is a modulated breathing of the O octahedra which causes band splitting by breaking the degeneracy of the crystal field between neighboring Mo sites. Finally, mode  $\nu = 13$  transforms like  $A_{2u}$  ( $M_4$ ) and therefore does not couple to splittings between  $E_g$  or  $T_{2g}$  states, explaining its insensitivity to the Hubbard  $U$ .